# Mathematic Analysis of Omnidirectional Wireless Power Transfer—Part-II Three-Dimensional Systems

Deyan Lin, *Member, IEEE*, Cheng Zhang, *Student Member, IEEE*, and S. Y. Ron Hui, *Fellow, IEEE*

***Abstract*—Part-II of this paper focuses on the mathematical analysis of the 3-D omnidirectional wireless power transfer (WPT) and also addresses the general principle of load detection. It provides the mathematical forms of distributions of the input power vector and output power vector, and demonstrates that the geometry of such 3-D distributed space follows the revolution of the Lemniscate of Bernoulli along its longitudinal axis. It provides the mathematical proof that the direction of energy transfer for the maximum energy efficiency is always in line with that of the maximum load power path in the 3-D space. Experimental verification is included to confirm the 3-D omnidirectional WPT theory.**

***Index Terms*—Magnetic resonance, omnidirectional wireless power, wireless power transfer.**

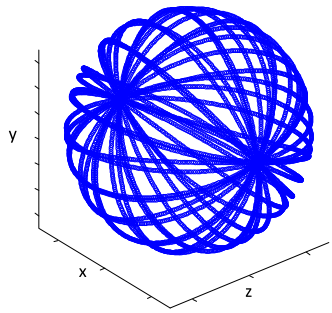


Fig. 1. Trajectory of the magnetic field vector at the center under controlling scheme proposed in [6] and [10].

## I. Introduction

WIRELESS power transfer (WPT) systems using magnetic coupling and resonance have been studied and used in many applications ranging from wireless charging of low power applications (such as medical implants [1] and portable electronics and [2]) to medium and high power application (such as mobile robots and electric vehicles [3]). The majority of practical implementations of wireless power systems involve "directional" power flow [4], [5]. Omnidirectional power transfer has been considered in [6]–[10]. O'Brien [6] and Jonah *et al*. [7] consider the use of three orthogonal coils to form an omnidirectional transmitter and similar three-orthogonal-coil structure as the receiver. The 3-D receiver structure, however, does not fit into many modern applications such as mobile phones and RFID tags that require a planar (2-D) receiver structure. Omnidirectional wireless power systems with planar receivers have been suggested in [8], [9], and [10]. It is noted that the WPT systems in [8] and [9] are operated at about 10.8 and 190 MHz, respectively. Such RF operation requires expensive RF power amplifier to drive the transmitter coils. The WPT in [10] adopts a sub-Mega Hertz operation and can be easily implemented with existing and low-cost switched mode power supply technology. While the current control method in [8] does not offer genuine omnidirectional feature, such limitation has recently been dealt with in [10].

While generating magnetic field in an omnidirectional manner offers great flexibility in free-positioning of the loads in a 3-D manner, such approach has been previously known to be energy inefficient. The reason is that most of the magnet flux flows into regions without the loads. For example, the magnetic field is controlled to rotate in [6] and [10], covering the sphere to ensure that the planar receiving coil always picks up power from the transmitter regardless of its position near the transmitter, as shown in Fig. 1. However, it can been seen from Fig. 1 that the magnetic field vector points at the two pole areas more often than other areas. Thus, a receiver placed at the pole area and at other area will receive different amount of power.

A discrete magnetic field vector control method has been proposed and successfully implemented in a 3-D omnidirectional WPT system [10], [11] (Fig. 2). The omnidirectional power flow control method in [10] and [11] involves a "tracking" mechanism to detect the load positions omnidirectionally and a "firing" mechanism to focus the magnetic flux toward the targeted loads. This approach enables an omnidirectional wireless power system to transfer power in a highly efficient manner. The simulation and experimental plots of the input power and load power vectors exhibit a 3-D dipole structure. Although experimental results have been positive in confirming the control method, there is no theory that can fully describe this physical phenomenon so far. This theoretical gap is filled in this paper. This paper is an extended version of [16]. The theoretical basis of the characteristics observed in simulation and experimental results of the 3-D WPT system is provided. The analysis is believed to be the first comprehensive theory for 3-D omnidirectional WPT in accounting for the 3-D power vector plots and their relationship to energy efficiency.

Manuscript received August 20, 2015; revised October 28, 2015 and January 11, 2016; accepted January 20, 2016. Date of publication January 29, 2016; date of current version September 16, 2016. This work was supported by the General Research Fund of the Hong Kong Research Grant Council under Project HKU 17206715. Recommended for publication by Associate Editor M. Duffy.

D. Lin and C. Zhang are with the Department of Electrical and Electronic Engineering, The University of Hong Kong, Pokfulam, Hong Kong (e-mail: deyanlin@eee.hku.hk; czhang@eee.hku.hk).

S. Y. R. Hui is with the Department of Electrical and Electronic Engineering, Imperial College London, London SW7 2AZ, U.K., and also with the Department of Electrical and Electronic Engineering, The University of Hong Kong, Pokfulam, Hong Kong (e-mail: ronhui@eee.hku.hk).

Color versions of one or more of the figures in this paper are available online at http://ieeexplore.ieee.org.

Digital Object Identifier 10.1109/TPEL.2016.2523506

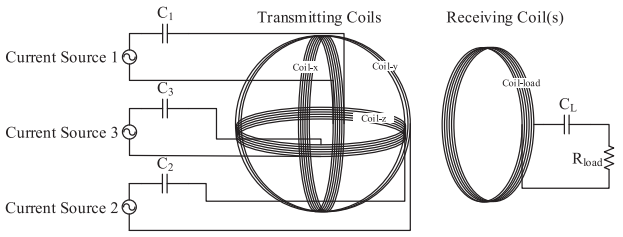


Fig. 2. Three-orthogonal-coil structure for the proposed omnidirectional WPT control method.

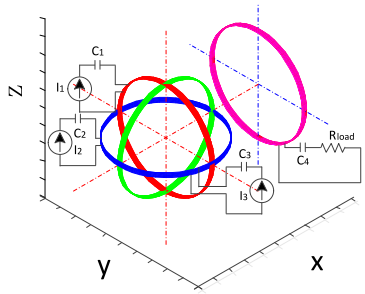


Fig. 3. Three-dimensional omnidirectional WPT system comprising three orthogonal transmitter coils and a receiver coil.

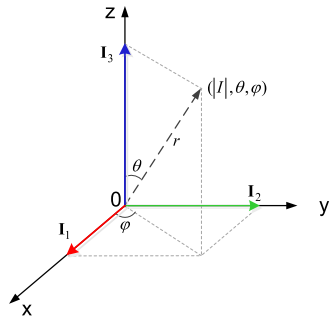


Fig. 4. Amplitude modulation description of current $\mathbf{I}_1$, $\mathbf{I}_2$, and $\mathbf{I}_3$, where $|I|$ is the magnitude of sinusoidal ac current $I$ (a) the resultant current vector sphere (b) the example of input current vector.

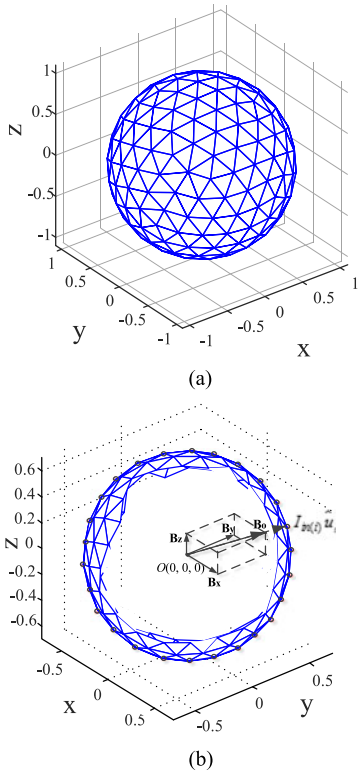


Fig. 5. Current vector plotted in space. (a) the resultant current vector sphere, (b) the example of input current vector.

TABLE I
$\theta$ AND $\varphi$ FOR FIG. 6

| Time ($10^{-4}$s) | $\theta$ | $\varphi$ | $\frac{I_1}{\lvert I\rvert}$ | $\frac{I_2}{\lvert I\rvert}$ | $\frac{I_3}{\lvert I\rvert}$ |
|---|---|---|---|---|---|
| t1: 0.0–0.5 | 30° | 30° | 0.433 | 0.250 | 0.866 |
| t2: 0.5–1.0 | 45° | 30° | 0.612 | 0.354 | 0.707 |
| t3: 1.0–1.5 | 60° | 45° | 0.612 | 0.612 | 0.500 |
| t4: 1.5–2.0 | 60° | 60° | 0.433 | 0.750 | 0.500 |

## II. 3-D Omnidirectional WPT System Analysis

A WPT system comprising three orthogonal transmitter coils and one receiver coil is shown in Fig. 3. Let the first (Red), the second (Green), and the third (Blue) coil be the transmitter coils orthogonal to each other, and the fourth (Red) coil be the receiver coil. The three transmitter coils are fed with ac current sources $\mathbf{I}_1$, $\mathbf{I}_2$, and $\mathbf{I}_3$ through current control at the same frequency that defines the rotating frequency of the resultant magnetic field. For genuine omnidirectional WPT, nonidentical current control must be adopted [6], [11], [12]. Based on the current amplitude control [12], the three currents in the three transmitter coils are set as

$$\begin{bmatrix} \mathbf{I}_1 \\ \mathbf{I}_2 \\ \mathbf{I}_3 \end{bmatrix} = \begin{bmatrix} \sin\theta\cos\varphi \\ \sin\theta\sin\varphi \\ \cos\theta \end{bmatrix} I \tag{1}$$

where $\theta$ and $\varphi$ are the angles related to the resultant current vectorin a spherical coordinate system as shown in Fig. 4 and $I$ is a sinusoidal time function. In (1), the amplitude modulation functions of these three currents in the column vector are set in this manner for a "per-unit" current vector system because $(\sin\theta\cos\varphi)^2 + (\sin\theta\sin\varphi)^2 + (\cos\theta)^2 = 1$. It should be stressed that there are various forms of current amplitude control for omnidirectional WPT systems. The choice of the three amplitude modulation functions in (1) is made simply to simplify the following analysis in a per-unit system.

These three current vectors $\mathbf{I}_1$, $\mathbf{I}_2$, and $\mathbf{I}_3$ will form a resultant unity current "vector" which will in turn generate a resultant magnetic field vector. Such magnetic vector will point at the same direction of the resultant current vector in Fig. 4. Non-identical current control has been proposed to control $\theta$ and $\varphi$ in (1) in order to direct the resultant magnetic vector to point at evenly distributed discrete points over the surface of a spherical surface as shown in Fig. 5. When the current vector can be controlled to point at any of the $N$ points that form the sphere, omnidirectional WPT can be achieved [11]. Since the angles $\theta$ and $\varphi$ can be used to control the direction of the resultant current vector, they are the control variables to control the direction of the magnetic field vector. Table I shows four different vector

directions defined by four sets of $\theta$ and $\varphi$. The three current amplitudes for these four directions are plotted in Fig. 6. It can be seen that in all cases, the amplitudes of the three currents are not identical.

If the magnetic vector is controlled to scan over all the points ($N = 200$) representing the spherical surface in sequence, the amplitude modulation functions of $I_1$, $I_2$, and $I_3$ can be seen in Fig. 7. Here, we assume that the scanning starts at the top of the spherical surface. The sphere can be "sliced" into several layers. So the amplitude modulation function of $I_3$ (i.e., cos$\theta$) moves down in discrete steps in Fig. 7. As the layer moves from the top to the equator of the sphere, the circumference increases and is thus represented by more points. Then, such circumference decreases progressively as the layer moves down to the bottom of the spherical surface. For each layer (i.e., with a constant $\theta$), the amplitude modulation functions of $I_2$ and $I_3$ are sinusoidal functions of $\varphi$ as shown in Fig. 7.

Assuming $L_i$ is the self inductance of the *i*th coil, $R_i$ is the coil resistance of the *i*th coil, and $M_{\rm ij}$ is the mutual inductance between the *i*th coil and the *j*th coil, the magnetically coupled coil system could be described in matrix equation [Eqn. (2) shown at the bottom of the page].

In (2), $\mathbf{U}_1$, $\mathbf{U}_2$, and $\mathbf{U}_3$ are the voltages of the current sources $\mathbf{I}_1$, $\mathbf{I}_2$, and $\mathbf{I}_3$. In general, all the parameters in the matrix equation (2) are known (e.g., $L_i, R_i$ and $M_{\rm ij}$ could be measured or calculated [14]; $C_i$ and $R_{\rm load}$ could be measured or identified by evolutionary approach using measured input voltages and currents at transmitter side [15]). The currents of the three current sources $\mathbf{I}_1$, $\mathbf{I}_2$, and $\mathbf{I}_3$, and their angular frequency $\omega$ are controlled by the transmitter circuit. Thus, $\mathbf{U}_1$, $\mathbf{U}_2$, $\mathbf{U}_3$, and $\mathbf{I}_4$, as well as the power flow from the three transmitters to the receiver and the overall efficiency of power transmission can be calculated.

In Fig. 5(a), each node represents an input current "vector" $\mathbf{I}_{\rm in(i)}$, which has three components: $I_1$, $I_2$, and $I_3$, with the same frequency and phase, and $\sqrt{I_1^2 + I_2^2 + I_3^2} = I^2$, where $I$ is a constant value. In 3-D space as shown in Fig. 5(a), a node with coordinates ($I_1$, $I_2$, $I_3$) is used to represent three current components $I_1$, $I_2$, $I_3$ for the first, the second, and the third transmitter coil, respectively. Since the magnitude of the vector for each node being the same, one can choose a large number (*N*) of uniformly distributed nodes in a spherical surface as the targeted points for power transfer. If the magnetic vector generated by the three transmitter coil currents can be directed at any of these *N* points, omnidirectional WPT can be achieved. For $N = 200$, Fig. 5(b) shows the *i*th node and the input current vector with magnitude *I*, and direction defined by unit vector $u_i$, where

$$\hat{u}_i = \left(\frac{I_{1i}}{I}, \frac{I_{2i}}{I}, \frac{I_{3i}}{I}\right) \tag{3}$$

and

$$\mathbf{I}_{\rm in(}_{i}{\rm )} = I_{\rm in(}_{i}{\rm )}\hat{u}_i \tag{4}$$

Since the first coil, the second coil, and the third coil of the transmitter are orthogonal to each other, $M_{12} = M_{13} = M_{23} = 0$, so (2) could be rewritten as [Eqn. (5) shown at the bottom of page].

Substituting (1) into (5) leads to [Eqn. (6) shown at the bottom of page].

$$\begin{bmatrix} \mathbf{U}_1 \\ \mathbf{U}_2 \\ \mathbf{U}_3 \\ 0 \end{bmatrix} = \begin{bmatrix} R_1 + j\left(\omega L_1 - \dfrac{1}{\omega C_1}\right) & j\omega M_{12} & j\omega M_{13} & j\omega M_{14} \\ j\omega M_{12} & R_2 + j\left(\omega L_2 - \dfrac{1}{\omega C_2}\right) & j\omega M_{23} & j\omega M_{24} \\ j\omega M_{13} & j\omega M_{23} & R_3 + j\left(\omega L_3 - \dfrac{1}{\omega C_3}\right) & j\omega M_{34} \\ j\omega M_{14} & j\omega M_{24} & j\omega M_{34} & R_4 + R_{\rm load} + j\left(\omega L_4 - \dfrac{1}{\omega C_4}\right) \end{bmatrix} \begin{bmatrix} \mathbf{I}_1 \\ \mathbf{I}_2 \\ \mathbf{I}_3 \\ \mathbf{I}_4 \end{bmatrix} \tag{2}$$

$$\begin{bmatrix} \mathbf{U}_1 \\ \mathbf{U}_2 \\ \mathbf{U}_3 \\ 0 \end{bmatrix} = \begin{bmatrix} R_1 + j\left(\omega L_1 - \dfrac{1}{\omega C_1}\right) & 0 & 0 & j\omega M_{14} \\ 0 & R_2 + j\left(\omega L_2 - \dfrac{1}{\omega C_2}\right) & 0 & j\omega M_{24} \\ 0 & 0 & R_3 + j\left(\omega L_3 - \dfrac{1}{\omega C_3}\right) & j\omega M_{34} \\ j\omega M_{14} & j\omega M_{24} & j\omega M_{34} & R_4 + R_{\rm load} + j\left(\omega L_4 - \dfrac{1}{\omega C_4}\right) \end{bmatrix} \begin{bmatrix} \mathbf{I}_1 \\ \mathbf{I}_2 \\ \mathbf{I}_3 \\ \mathbf{I}_4 \end{bmatrix} \tag{5}$$

$$\begin{bmatrix} \mathbf{U}_1 \\ \mathbf{U}_2 \\ \mathbf{U}_3 \\ 0 \end{bmatrix} = \begin{bmatrix} R_1 + jX_1 & 0 & 0 & j\omega M_{14} \\ 0 & R_2 + jX_2 & 0 & j\omega M_{24} \\ 0 & 0 & R_3 + jX_3 & j\omega M_{34} \\ j\omega M_{14} & j\omega M_{24} & j\omega M_{34} & R_4 + R_{\rm load} + jX_4 \end{bmatrix} \begin{bmatrix} I\sin\theta\cos\varphi \\ I\sin\theta\sin\varphi \\ I\cos\theta \\ \mathbf{I}_4 \end{bmatrix} \tag{6}$$

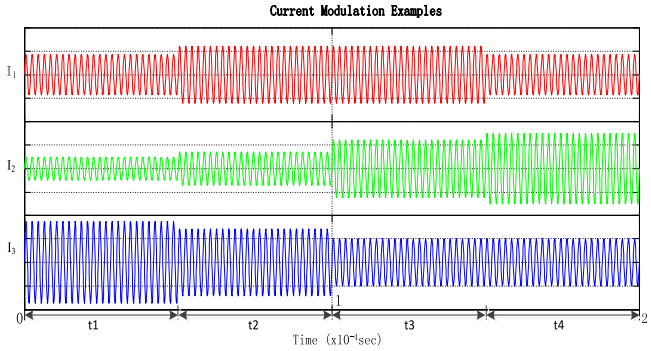


Fig. 6. Amplitudes of current $\mathbf{I}_1$, $\mathbf{I}_2$, and $\mathbf{I}_3$ at the four different directions specified in Table I based on (1).

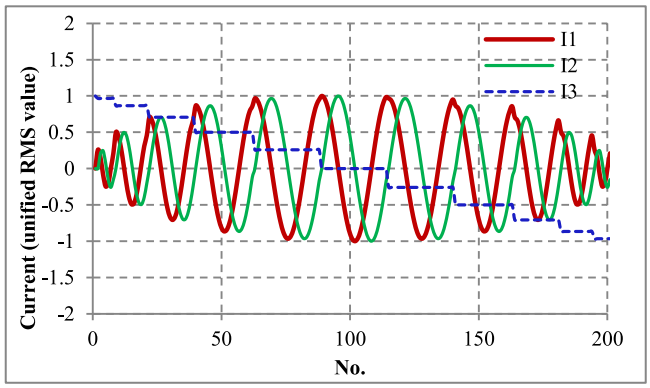


Fig. 7. Variations of the amplitude modulation functions of (1) as the magnetic field vector moves from the top of the spherical surface progressively in discrete steps to the bottom of the spherical surface.

where

$$X_1 = \left(\omega L_1 - \frac{1}{\omega C_1}\right), X_2 = \left(\omega L_2 - \frac{1}{\omega C_2}\right),$$
$$X_3 = \left(\omega L_3 - \frac{1}{\omega C_3}\right), X_4 = \left(\omega L_4 - \frac{1}{\omega C_4}\right).$$

### A. Load Current Calculation

The last equation in (6) that is related to the load current $\mathbf{I}_4$ can be expressed as

$$j\omega M_{14} I \sin\theta\cos\varphi + j\omega M_{24} I \sin\theta\sin\varphi + j\omega M_{34} I\cos\theta + (R_4 + R_{\text{load}} + jX_4)\mathbf{I}_4 = 0. \quad (7)$$

Putting $\mathbf{I}_4$ as the subject of the equation

$$\mathbf{I}_4 = -\frac{j\omega I}{R_4 + R_{\text{load}} + jX_4} \times (M_{14}\sin\theta\cos\varphi + M_{24}\sin\theta\sin\varphi + M_{34}\cos\theta) \quad (8)$$

where the amplitude is

$$I_4 = \frac{\omega I}{\sqrt{(R_4 + R_{\text{load}})^2 + X_4^2}} \times |M_{14}\sin\theta\cos\varphi + M_{24}\sin\theta\sin\varphi + M_{34}\cos\theta| \quad (9)$$

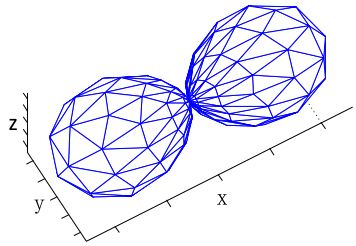


Fig. 8. Load power: The surface of revolution of Lemniscate of Bernoulli along the longitudinal axis.

### B. Output Power Calculation

*1) $P_{\text{load}}$: Load Power*

With the expression of load current determined, the output power can be obtained as follows

$$P_{\text{load}} = I_4^2 R_{\text{load}} = \frac{\omega^2 I^2 R_{\text{load}}}{(R_4 + R_{\text{load}})^2 + X_4^2} \times (M_{14}\sin\theta\cos\varphi + M_{24}\sin\theta\sin\varphi + M_{34}\cos\theta)^2 \quad (10)$$

The load power in (10) can be plotted as the surface of revolution of Lemniscate of Bernoulli along the longitudinal axis as shown in Fig. 8. It has a dumbbell shape.

The output power equation can further be expanded as

$$\begin{aligned} P_{\text{load}} &= \frac{\omega^2 I^2 R_{\text{load}}}{(R_4 + R_{\text{load}})^2 + X_4^2} \times (M_{14}\sin\theta\cos\varphi + M_{24}\sin\theta\sin\varphi + M_{34}\cos\theta)^2 \\ &= \frac{\omega^2 I^2 R_{\text{load}}}{(R_4 + R_{\text{load}})^2 + X_4^2} \left(\sqrt{M_{14}^2 + M_{24}^2} \times \sin\left(\arctan\frac{M_{14}}{M_{24}} + \varphi\right)\sin\theta + M_{34}\cos\theta\right)^2 \\ &= \frac{\omega^2 I^2 R_{\text{load}}}{(R_4 + R_{\text{load}})^2 + X_4^2} \left((M_{14}^2 + M_{24}^2) \times \sin^2\left(\arctan\frac{M_{14}}{M_{24}} + \varphi\right) + M_{34}^2\right)\sin^2(\gamma_{3-D} + \theta) \\ &= I^2 R_{\text{load}} K_{3-D(\varphi)} \sin^2(\gamma_{3-D} + \theta) \end{aligned} \quad (11)$$

where

$$\gamma_{3-D} = \arctan\frac{M_{34}}{\sqrt{M_{14}^2 + M_{24}^2}\sin\left(\arctan\frac{M_{14}}{M_{24}} + \varphi\right)} \quad (12)$$

$$K_{3-D(\varphi)} = \frac{\omega^2\left((M_{14}^2 + M_{24}^2)\sin^2\left(\arctan\frac{M_{14}}{M_{24}} + \varphi\right) + M_{34}^2\right)}{(R_4 + R_{\text{load}})^2 + X_4^2}. \quad (13)$$

When $\sin^2\left(\arctan\frac{M_{14}}{M_{24}} + \varphi\right) = 1$ and $\sin^2(\gamma_{3-D} + \theta) = 1$, i.e., $\arctan\frac{M_{14}}{M_{24}} + \varphi = \frac{\pi}{2}$ or $\frac{3\pi}{2}$, and $\gamma_{3-D} + \theta = \frac{\pi}{2}$ or $\frac{3\pi}{2}$, $P_{\text{load}}$ reaches its maximum value

$$P_{\text{load\_max}} = I^2 K_{3-D} R_{\text{load}} \quad (14)$$

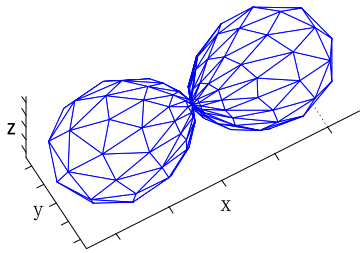


Fig. 9. Power picked up by the receiver: The surface of revolution of Lemniscate of Bernoulli curve along the longitudinal axis.

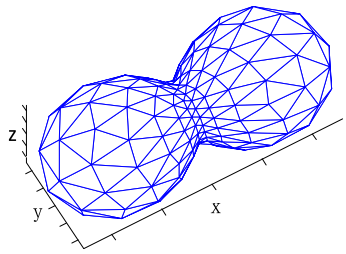


Fig. 10. Total input power of the three transmitters: The surface of revolution of deformed Lemniscate of Bernoulli along the longitudinal axis.

where

$$K_{3-D} = \frac{\omega^2\left(M_{14}^2 + M_{24}^2 + M_{34}^2\right)}{(R_4 + R_{\rm load})^2 + X_4^2} \tag{15}$$

When $\sin^2(\gamma_{3-D} + \theta) = 0$, i.e., $\gamma_{3-D} + \theta = 0\,\text{or}\,\pi$, $P_{\rm load}$ reaches its minimum value

$$P_{\rm load\_min} = 0 \tag{16}$$

*2) $P_{\rm out}$: Power Picked Up by the Receiver:*

The output power is equal to the sum of the conduction power loss in the receiver resonant-coil and the load power

$$\begin{aligned} P_{\rm out} &= I_4^2 R_4 + I_4^2 R_{\rm load} \\ &= \frac{\omega^2 I^2 (R_4 + R_{\rm load})}{(R_4 + R_{\rm load})^2 + X_4^2} \\ &\quad \times (M_{14}\sin\theta\cos\varphi + M_{24}\sin\theta\sin\varphi + M_{34}\cos\theta)^2 \\ &= I^2 (R_4 + R_{\rm load}) K_{3-D(\varphi)} \sin^2(\gamma_{3-D} + \theta) \end{aligned} \tag{17}$$

Equation (17) also follows the surface of revolution of Lemniscate of Bernoulli along the longitudinal axis as shown in Fig. 9. The volume of this dumbbell shaped figure is slightly larger than that of the load power as shown in Fig. 8, because it includes the $I_4^2 R_4$ term.

When $\sin^2\left(\arctan\frac{M_{14}}{M_{24}} + \varphi\right) = 1$ and $\sin^2(\gamma_{3-D} + \theta) = 1$, i.e., $\arctan\frac{M_{14}}{M_{24}} + \varphi = \frac{\pi}{2}$ or $\frac{3\pi}{2}$, and $\gamma_{3-D} + \theta = \frac{\pi}{2}$ or $\frac{3\pi}{2}$, $P_{\rm out}$ reaches its maximum value

$$P_{\rm out\_max} = I^2 K_{3-D} (R_4 + R_{\rm load}) \tag{18}$$

When $\sin^2(\gamma_{3-D} + \theta) = 0$, i.e.,$\gamma_{3-D} + \theta = 0\,\text{or}\,\pi$, $P_{\rm out}$ reaches its minimum value

$$P_{\rm out\_min} = 0 \tag{19}$$

### C. Input Power Calculation

The input power is the sum of the conduction power losses in the transmitter and receiver coils and the load power

$$P_{\rm loss1} = I_1^2 R_1 = I^2 R_1 \sin^2\theta\cos^2\varphi \tag{20}$$

$$P_{\rm loss2} = I_2^2 R_2 = I^2 R_2 \sin^2\theta\sin^2\varphi \tag{21}$$

$$P_{\rm loss3} = I_3^2 R_3 = I^2 R_3 \cos^2\theta \tag{22}$$

$$P_{\rm loss4} = I_4^2 R_4 \tag{23}$$

$$P_{\rm load} = I_4^2 R_{\rm load} \tag{24}$$

$$\begin{aligned} P_{\rm in} &= P_{\rm loss1} + P_{\rm loss2} + P_{\rm loss3} + P_{\rm loss4} + P_{\rm load} \\ &= I^2 R_1 \sin^2\theta\cos^2\varphi + I^2 R_2 \sin^2\theta\sin^2\varphi \\ &\quad + I^2 R_3 \cos^2\theta + I_4^2 R_4 + I_4^2 R_{\rm load} \end{aligned} \tag{25}$$

By substituting (9) into (25), equation (26) can be obtained

$$\begin{aligned} P_{\rm in} &= I^2 R_1 \sin^2\theta\cos^2\varphi + I^2 R_2 \sin^2\theta\sin^2\varphi + I^2 R_3 \cos^2\theta \\ &\quad + \frac{\omega^2 I^2 (R_4 + R_{\rm load})}{(R_4 + R_{\rm load})^2 + X_4^2} \\ &\quad \times (M_{14}\sin\theta\cos\varphi + M_{24}\sin\theta\sin\varphi + M_{34}\cos\theta)^2 \end{aligned} \tag{26}$$

$$\begin{aligned} \text{If } R_1 &= R_2 = R_3 = R, \\ P_{\rm in} &= I^2 R + \frac{\omega^2 I^2 (R_4 + R_{\rm load})}{(R_4 + R_{\rm load})^2 + X_4^2} \\ &\quad \times (M_{14}\sin\theta\cos\varphi + M_{24}\sin\theta\sin\varphi + M_{34}\cos\theta)^2 \\ &= I^2 R + P_{\rm out} \\ &= I^2 R + I^2 (R_4 + R_{\rm load}) K_{3-D(\varphi)} \sin^2(\gamma_{3-D} + \theta) \end{aligned} \tag{27}$$

When $\sin^2\left(\arctan\frac{M_{14}}{M_{24}} + \varphi\right) = 1$ and $\sin^2(\gamma_{3-D} + \theta) = 1$, i.e., $\arctan\frac{M_{14}}{M_{24}} + \varphi = \frac{\pi}{2}$ or $\frac{3\pi}{2}$, and $\gamma_{3-D} + \theta = \frac{\pi}{2}$ or $\frac{3\pi}{2}$, $P_{\rm in}$ reaches its maximum value

$$P_{\rm in\_max} = I^2 R + I^2 K_{3-D} (R_4 + R_{\rm load}) \tag{28}$$

When $\sin^2(\gamma_{3-D} + \theta) = 0$, i.e., $\gamma_{3-D} + \theta = 0\,\text{or}\,\pi$, $P_{\rm in}$ reaches its minimum value

$$P_{\rm in\_min} = I^2 R \tag{29}$$

The input power in (24) can be represented as a 3-D dumbbell-shaped figure as shown in Fig. 10. Its surface is formed by the revolution of deformed Lemniscate of Bernoulli along the longitudinal axis.

### D. Efficiency Calculation

The energy efficiency is equal to the ratio of the load power and the input power

$$\eta = \frac{P_{\text{load}}}{P_{\text{in}}} = \frac{I^2 R_{\text{load}} K_{3-D(\varphi)} \sin^2(\gamma_{3-D}+\theta)}{I^2 R + I^2 (R_4 + R_{\text{load}}) K_{3-D(\varphi)} \sin^2(\gamma_{3-D}+\theta)}$$
$$= \frac{R_{\text{load}} K_{3-D(\varphi)} \sin^2(\gamma_{3-D}+\theta)}{R + (R_4 + R_{\text{load}}) K_{3-D(\varphi)} \sin^2(\gamma_{3-D}+\theta)} \quad (30a)$$

or

$$\eta = \frac{R_{\text{load}}}{\frac{R}{K_{3-D(\varphi)} \sin^2(\gamma_{3-D}+\theta)} + (R_4 + R_{\text{load}})} \quad (30b)$$

When $\sin^2\left(\arctan\frac{M_{14}}{M_{24}} + \varphi\right) = 1$ and $\sin^2(\gamma_{3-D}+\theta) = 1$, i.e., $\arctan\frac{M_{14}}{M_{24}} + \varphi = \frac{\pi}{2}$ or $\frac{3\pi}{2}$, and $\gamma_{3-D} + \theta = \frac{\pi}{2}$ or $\frac{3\pi}{2}$, $\eta$ reaches its maximum value, just as $P_{\text{in}}$ does

$$\eta_{\max} = \frac{R_{\text{load}}}{\frac{R}{K_{3-D}} + (R_4 + R_{\text{load}})} \quad (31)$$

When $\sin^2(\gamma_{3-D}+\theta) = 0$, i.e., $\gamma_{3-D} + \theta = 0$ or $\pi$, $\eta$ reaches its minimum value

$$\eta_{\min} = 0 \quad (32)$$

## III. Dumbbell-Shaped Input Power Vector Plot and its Implications to Energy Efficiency and Load Direction

The analysis in Section II has important implications to the energy efficiency and load power direction. Equations (14), (28), and (31) indicate that the maximum values of the 1) load power, 2) input power, and 3) energy efficiency reach their respective maximum under two conditions :

1) $\sin^2\left(\arctan\frac{M_{14}}{M_{24}} + \varphi\right) = 1 \Rightarrow \arctan\frac{M_{14}}{M_{24}} + \varphi = \frac{\pi}{2}$ or $\frac{3\pi}{2}$.
2) $\sin^2(\gamma_{3-D}+\theta) = 1 \Rightarrow \gamma_{3-D} + \theta = \frac{\pi}{2}$ or $\frac{3\pi}{2}$.

(Note: the direction of the maximum load power means the direction at which the load will receive maximum power. It may not be identical to the physical dimension of the load itself.)

Two important conclusions can be drawn here. First, sending the wireless power directly toward the targeted load power direction is the most energy efficient method instead of sending power to all directions. Second, such maximum load power direction can be determined from the input power. Because only the input power information is needed, control of the power flow can theoretically be done on the transmitter side (without wireless feedback from the load).

### A. Mathematical Method

The use of the input power is of particular significance, because it can be measured on the transmitter circuit without monitoring the loads. Therefore, the total input power plot can be used to predict the maximum points for the load power, output power, and efficiency, as well as the load direction as shown in Fig. 11. Since $\omega$, $I$, $R$, $R_4$, $X_4$ are known or could be measured previously, and $\varphi$ could be fixed for the ease of resolving subsequent equation set, there are only $M_{14}$, $M_{24}$, $M_{34}$, and *Rload* to be identified in (27). Note the $K_{3-D(\varphi)}$ in (13) consists of these four unknowns and $\gamma_{3-D}$ consists of the three unknown mutual coupling terms in (12). The four unknowns in the input power function can be calculated in four measurements of total input power at different $\theta_1, \theta_2, \theta_3, \theta_4$ theoretically as shown in (33). As the output power and the energy efficiency plots are surfaces formed by the revolution Lemniscates of Bernoulli with the same longitudinal axis, the direction of the maximum load power and thus the maximum energy efficiency can be determined analytically

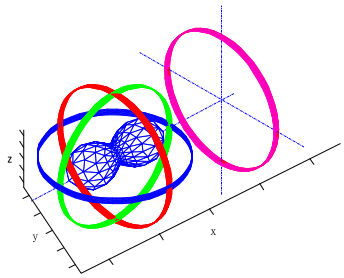


Fig. 11. Position of the dumbbell-shaped input power plot in the presence of a loaded receiver coil-resonator.

$$\begin{cases} P_{\text{in}}(\theta_1) = I^2 R + K_{3-D(\varphi)} I^2 (R_4 + R_{\text{load}}) \sin^2(\gamma_{3-D}+\theta_1) \\ P_{\text{in}}(\theta_2) = I^2 R + K_{3-D(\varphi)} I^2 (R_4 + R_{\text{load}}) \sin^2(\gamma_{3-D}+\theta_2) \\ P_{\text{in}}(\theta_3) = I^2 R + K_{3-D(\varphi)} I^2 (R_4 + R_{\text{load}}) \sin^2(\gamma_{3-D}+\theta_3) \\ P_{\text{in}}(\theta_4) = I^2 R + K_{3-D(\varphi)} I^2 (R_4 + R_{\text{load}}) \sin^2(\gamma_{3-D}+\theta_4) \end{cases} \quad (33)$$

### B. 2-Plane Method

An alternative way to find the maximum point for input power is to use two perpendicular 2-D planes for cutting the dumbbell-shaped input power plot, on the condition that these two perpendicular planes cut through the origin. The intersection of a flat 2-D plane and the surface of the input power vector plot will form a deformed Lemniscate of Bernoulli. The full analysis for this method is provided in the Appendix. The procedure of this approach for finding the angle of the maximum input power is:

1) Choosing a plane which passes through the origin of the curved surface of input power vector plot. The intersection of the 2-D plane and the 3-D surface should be deformed Lemniscate of Bernoulli curve as shown in Fig. 12 (as an example, the *XY* plane is chosen here).
2) Choose two current vectors belonging to the plane in Step 1, as shown in Fig. 13. Measure the total input power at these two points. The total input power curve versus the angle $\beta$ will be a sinusoidal waveform with a dc offset as shown in Fig. A1 with mathematical proof in the Appendix. As an example, $\beta = 0$ and $\beta = \frac{\pi}{2}$ are chosen as the angles of these two chosen current vectors in Fig. 13. Then, one can calculate the "local" maximum input power direction on this plane. This local maximum input power point is the projection of the "global" maximum input power point on the chosen 2-D plane.

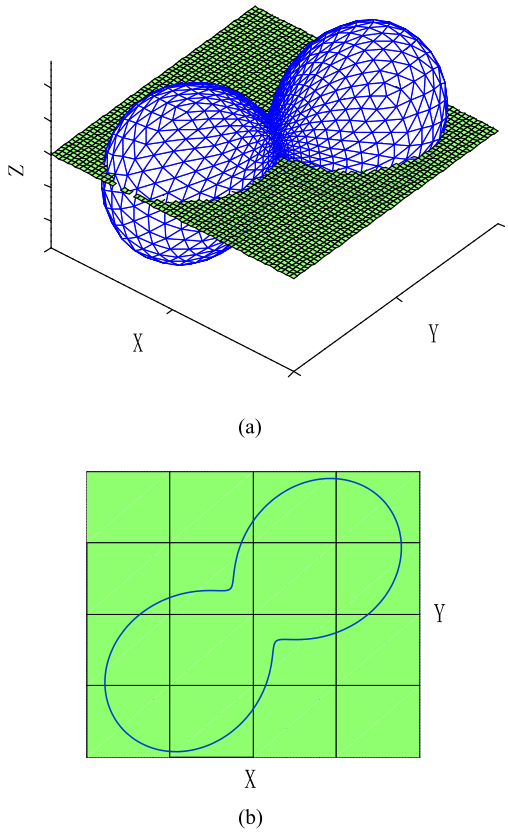


Fig. 12. (a) 3-D diagram and (b) 2-D diagram of the first plane passing through the origin of the curved surface of input power vector plot.

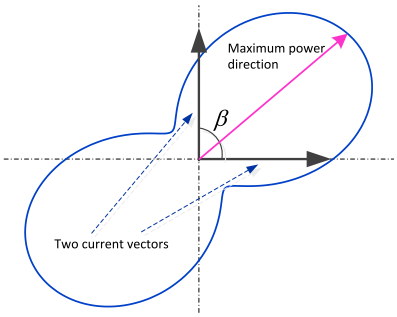


Fig. 13. Use of two current vectors to determine the local maximum power on the first plane.

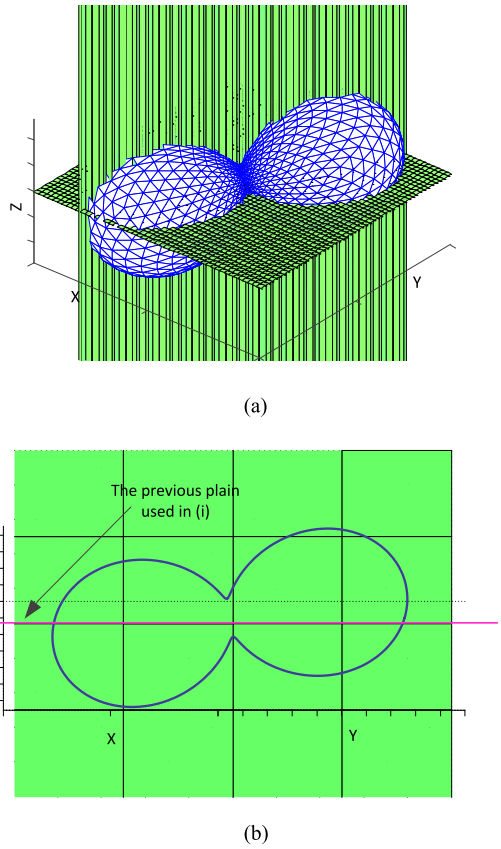


Fig. 14. (a) 3-D diagram and (b) 2-D diagram of the second plane (perpendicular to the first plane) passing through the origin of the curved surface of input power vector plot.

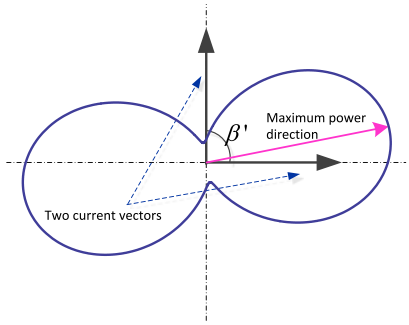


Fig. 15. Use of two current vectors to determine the global maximum power on the second plane.

3) Choose a second plane that is perpendicular to the first one and also passes through the origin. The intersection of this vertical plane with the 3-D surface of the input power plot will form another Lemniscate of Bernoulli as shown in Fig. 14. It also includes the maximum input power point calculated in Step 2.
4) Choose two current vectors belonging to the second plane in Step 3, as shown in Fig. 15. Measure the input powers at these two points. Again, the total input power curve versus the angle $\beta'$ will be a sinusoidal waveform with a dc offset. Then, one can determine the angle $\beta'_m$ on the second plane, at which the global maximum input power occurs. This is the direction of the global maximum input power point. This direction is in line with that for maximum energy efficiency.

## IV. Experimental Verifications

Some experiments have been conducted to verify the theoretical results in Section II. The parameters used for the experiments are: Transmitters' diameters: $d_1 = d_2 = d_3 = 0.3$ m, transmitter winding turns: $T_1 = T_2 = T_3 = 11$, the self-inductance of the three transmitters are $L_1 = L_2 = L_2 = 82.03$ $\mu$H, receiver

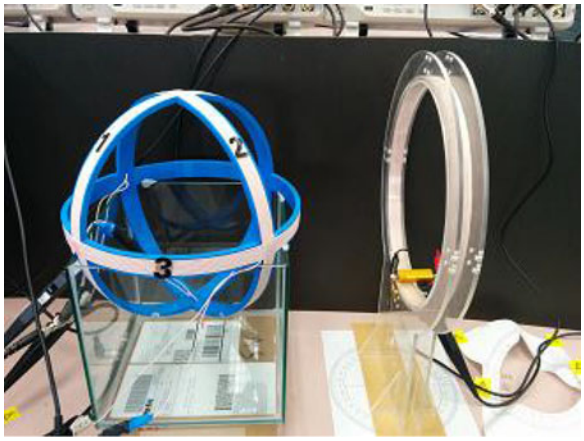

Fig. 16. Experiment setup.

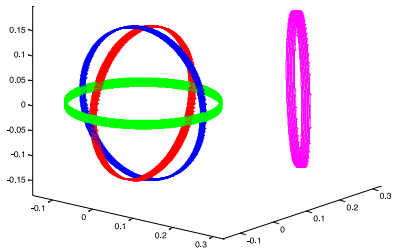

Fig. 17. Theoretical model: The coils are placed exactly the same location as the simulation model. Red, blue, green, and violate coils stands for transmitter x, y, z, and receiver coil, respectively.

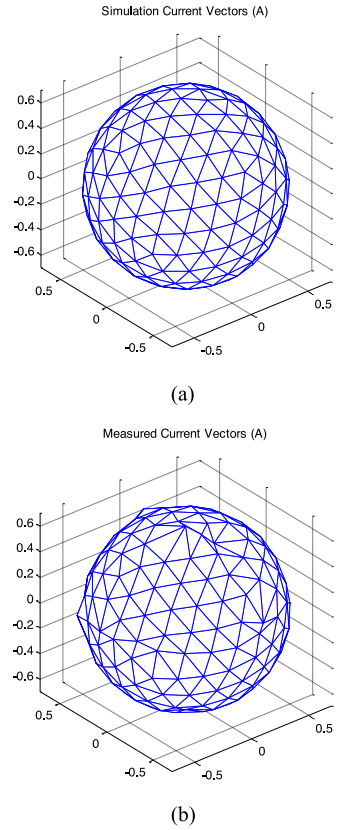


Fig. 18. Surfaces formed by the 200 evenly distributed (a) theoretical and (b) experimental current vectors in 3-D space.

coil diameter: $d_4 = 0.3$ m, receiver coil winding turns: $T_4 = 11$, the self-inductance of the receiver coil is $L_4 = 82.03$ $\mu$H, the distance between the centers of the transmitter and the receiver coil $d = 0.3$ m, $C_1 = C_2 = C_3 = C_4 = 1$ nF, transmitter coil resistance $R = 0.9998$ $\Omega$, receiver coil resistance $R_4 = 0.9998$ $\Omega$. $R_{\text{load}} = 10$ $\Omega$ and operating frequency f = 535 kHz ($\omega = 3.36 \times 10^6$ rad/s), $I = 0.424$ A.

Fig. 16 shows the experimental setup. The locations of the three transmitter coils and the receiver coil are shown in the Fig. 17. The physical coordinates are used to provide the theoretical results. The current amplitude control based on (1) is used to produce a unity current vector (and their resultant magnetic field vector) pointing at 200 evenly distributed points as shown in Fig. 18(a). The ability of pointing at these 200 directions by the magnetic field vector means that the transmitter system has the genuine omnidirectional wireless power feature. The practically measured transmitter coil currents are used to generate the practical magnetic field vector pointing at these 200 directions. The measured points are plotted in Fig. 18(b). The measurements are generally in good agreement with the theoretical results.

When such unity current vector (and its resultant magnetic field vector) is scanned over these 200 directions, the input power and the load power of each vector are calculated from the practical voltage and current measurements. The input power vector plot and the load power plot can then be constructed for comparison with the theoretical results.

Fig. 19(a) and (b) shows the theoretical and measured input power plots. Both of them exhibit the similar dumbbell shapes. The corresponding theoretical and measured plots of the load power are included in Fig. 20(a) and (b), respectively.

Tests have also been conducted to demonstrate the 2-plane method. The location of the receiver coil is placed with respect to the three-coil transmitter in the direction expressed in the per-unit vector as $\{0.7, 0.7, 0.14\}$ in Cartesian coordinate system. For simplicity, the $xy$ plane is chosen as the first plane. The normal of the first plane is therefore $n_1$: $\{0, 0, 1\}$ in Cartesian coordinate system. The currents of the three transmitting coils are adjusted so that the vector of the central magnetic field pivoted at the origin will rotate a complete cycle in discrete steps. The total input power values (not per-unit values) associated with the magnetic field vector in these discrete positions have been recorded. The trajectory of the input power vector based on 36 practical measurements on the first chosen $XY$ plane is plotted in Fig. 21. From this trajectory (which follows the shape of a deformed Lemniscate of Bernoulli as explained previously), the direction of the maximum power flow can be determined as about 47° on this $XY$ plane. Note that the per-unit $X$ and $Y$ coordinates of the load are 0.7 and 0.7. The theoretical angle of the maximum power flow should be 45°. However, considering the tolerances of the system parameters and measurement errors, the estimated angle of 47° on this $XY$ plane is in good agreement with the theoretical value of 45°. By displaying the trajectory

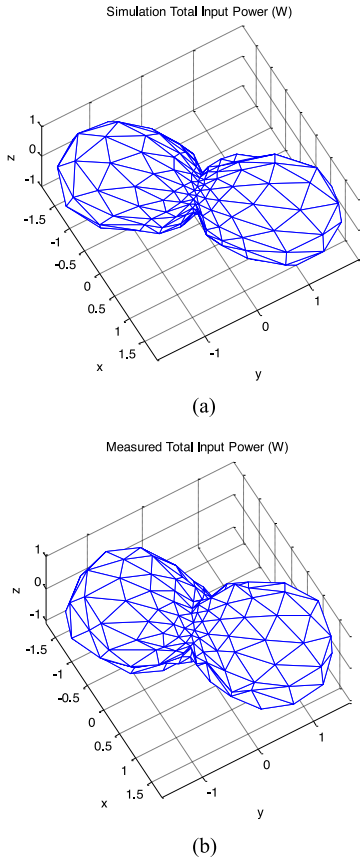


Fig. 19. Plots of the (a) theoretical and (b) experimental total input power vectors.

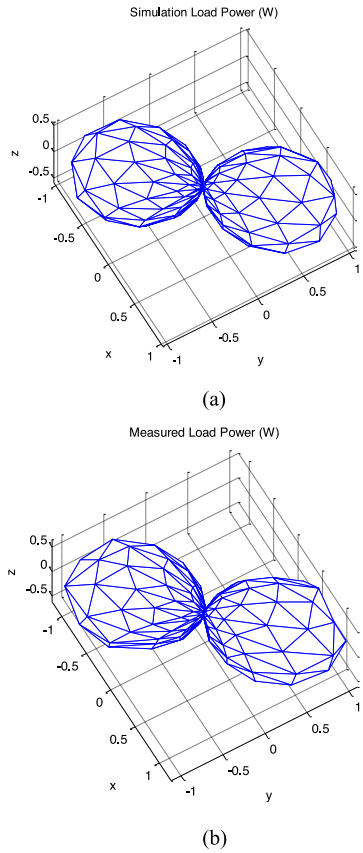


Fig. 20. Plots of the (a) theoretical and (b) experimental load power vectors.

of the corresponding energy efficiency with that of the input power vector, it can be seen from Fig. 22 that the direction of the maximum power flow is in line with that of the maximum energy efficiency. This set of practical results confirms the prediction of the theory.

With the direction of the maximum input power vector $P_1$ determined from the first plane, the second plane perpendicular to the first can be chosen. In this case, the normal of the second plane is $n_2 = n_1 \times P_1$. Labeling the $x$ and $y$ axes as $X'$ and $Y'$ for the second plane, the corresponding intersection points of this plane with the surface of the 3-D input power vector form a trajectory curve as shown in Fig. 23. From this plot, the maximum power vector has an angle of 77° from the new $Y'$-axis. The corresponding display of the input power and efficiency trajectories are given in Fig. 24. Based on these measurements and using the method included in the Appendix, the estimated load direction is found to be $\{0.67, 0.71, \text{and } 0.21\}$ in Cartesian coordinate system. Considering the tolerances of system parameters and measurement errors, this estimated load direction is consistent with the ideal set of $\{0.7, 0.7, \text{and } 0.14\}$.

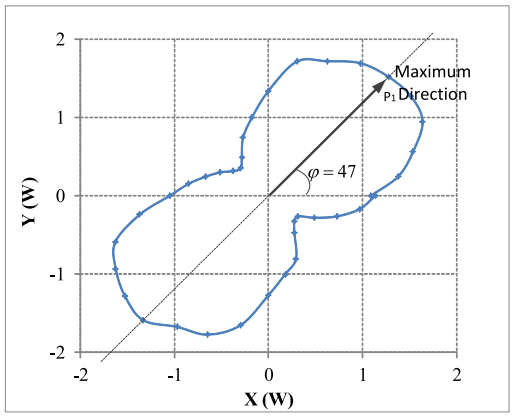


Fig. 21. Trajectory of the input power vector over one cycle on the first *XY* plane.

## V. Conclusion

Part-II of this paper deals with the theory for describing the relationships among the total input power, output power, and the energy efficiency for 3-D omnidirectional WPT systems. When the 3-D omnidirectional system is driven by a rotating current vector, the distributions of the total input power, load power, and the efficiency form surfaces of a revolution of Lemniscate of Bernoulli. It also shows that the direction of the maximum input power vector is the same as that of the maximum energy efficiency. This interesting feature provides a useful tool to detect the location of the load. A mathematical method and a 2-plane method have been proposed to determine this direction of load. Experiments have been conducted on a hardware prototype. The experimental results have confirmed the validity of the theory. This theory forms a theoretical foundation on which different

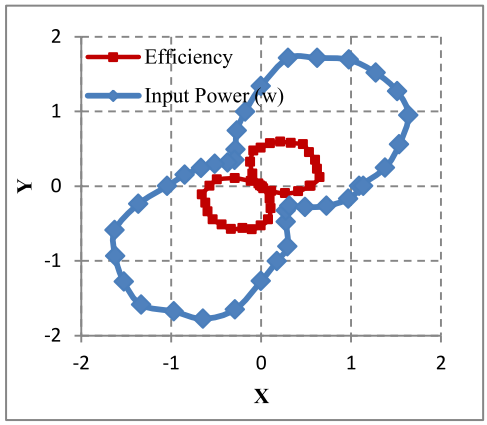


Fig. 22. Trajectories of the input power vector and energy efficiency over one cycle on the first *XY* plane. (Note: The first plane: $\varphi = 47°$, the normal of the plane is $n_1$: {0, 0, 1} in Cartesian coordinate system).

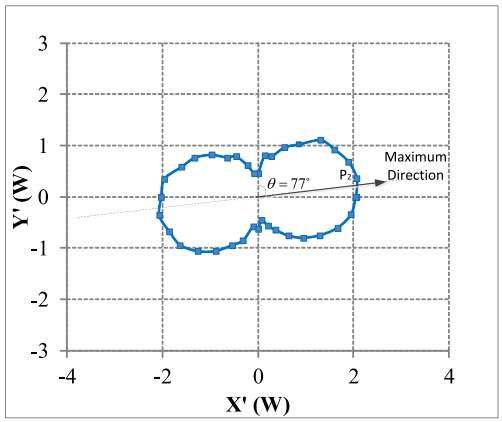


Fig. 23. Trajectory of the input power vector over one cycle on the second *XY* plane.

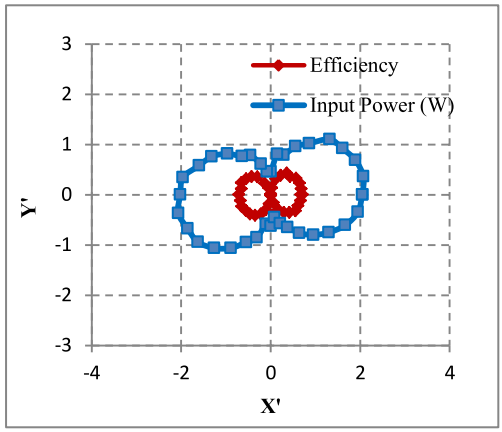


Fig. 24. Trajectories of the input power vector and energy efficiency over one cycle on the second *XY* plane. (Note: The second plane: $\theta = 77°$, the normal of the plane is $\{0.7314, -.6820, 0\}$ in Cartesian coordinate system).

control methods on such omnidirectional WPT system could be evaluated in the future.

## APPENDIX

The direction of the load can be obtained from the 2-plane method based on the measurements of the total input power $P_{\text{in}}$. To simplify the analysis, $P_{\text{out}}$ is used at first because the difference between $P_{\text{in}}$ and $P_{\text{out}}$ is only $I_2R$ according to (27). For the $P_{\text{out}}$ expression in (17), if using a plane to pass through the origin with normal $n = [abc]$ in Cartesian coordinate system and to cut the surface of the output power, one will get a curve defined by

$$\begin{cases} P_{\text{out}} = \dfrac{\omega^2 I^2 (R_4 + R_{\text{load}})}{(R_4 + R_{\text{load}})^2 + X_4^2} \\ \qquad \times (M_{14}\sin\theta\cos\varphi + M_{24}\sin\theta\sin\varphi + M_{34}\cos\theta)^2 \\ ax + by + cz = 0. \end{cases} \tag{34}$$

From Fig. 4, the relationship between the Cartesian coordinate system and the Spherical coordinate system should be (35) [13]

$$\begin{cases} x = r\sin\theta\cos\varphi \\ y = r\sin\theta\sin\varphi \\ z = r\cos\theta \\ r = \sqrt{x^2 + y^2 + z^2} \end{cases} \tag{35}$$

The value of $P_{\text{out}}$ in Cartesian coordinate system is exactly the same as that in Spherical coordinate *r*. So (34) can be transformed into the Cartesian coordinate system as

$$\begin{cases} P_{\text{out}} = r = K\left(M_{14}\dfrac{x}{r} + M_{24}\dfrac{y}{r} + M_{34}\dfrac{z}{r}\right)^2 \\ ax + bx + cx \end{cases} \tag{36}$$

That is

$$\begin{cases} P_{\text{out}} : \left(x^2 + y^2 + z^2\right)^{\frac{3}{2}} = K\left(M_{14}x + M_{24}y + M_{34}z\right)^2 \\ ax + by + cz = 0 \end{cases} \tag{37}$$

where

$$K = \frac{\omega^2 I^2 (R_4 + R_{\text{load}})}{(R_4 + R_{\text{load}})^2 + X_4^2} \tag{38}$$

In order to simplify the equation, a rotated coordinates system where the normal of the plane being $n' = \begin{bmatrix} 0 & 0 & \sqrt{a^2 + b + c^2} \end{bmatrix}$ can be used. This rotation will make the cutting plane to be the *XY* plane in the new coordinate system. The matrix formula used for rotating the normal vector and the plane is

$$n' = nAB = \begin{bmatrix} 0 & 0 & \sqrt{a^2 + b^2 + c^2} \end{bmatrix} \tag{39}$$

where

$$A = \begin{bmatrix} \dfrac{a}{\sqrt{b^2 + a^2}} & -\dfrac{b}{\sqrt{b^2 + a^2}} & 0 \\ \dfrac{b}{\sqrt{b^2 + a^2}} & \dfrac{a}{\sqrt{b^2 + a^2}} & 0 \\ 0 & 0 & 1 \end{bmatrix} \tag{40}$$

$$\begin{cases} P_{\text{out}} : (x'^2 + y'^2 + z'^2)^{\frac{3}{2}} \\ = K \left( \dfrac{\begin{array}{l}(acM_{14} + bcM_{24} - (a^2+b^2)M_{34})x' + (a\sqrt{a^2+b^2+c^2}M_{24} - b\sqrt{a^2+b^2+c^2}M_{14})y' \\ + (a\sqrt{a^2+b^2}M_{14} + b\sqrt{a^2+b^2}M_{24} + \sqrt{a^2+b^2}cM_{34})z'\end{array}}{\sqrt{a^2+b^2}\sqrt{a^2+b^2+c^2}} \right)^2 \\ z' = 0 \end{cases} \tag{43}$$

$$B = \begin{bmatrix} \dfrac{c}{\sqrt{c^2+b^2+a^2}} & 0 & \dfrac{\sqrt{b^2+a^2}}{\sqrt{c^2+b^2+a^2}} \\ 0 & 1 & 0 \\ -\dfrac{\sqrt{b^2+a^2}}{\sqrt{c^2+b^2+a^2}} & 0 & \dfrac{c}{\sqrt{c^2+b^2+a^2}} \end{bmatrix} \tag{41}$$

Every point $p(x, y, z)$ in old coordinate system will be rotated as well. The new coordinates $p'(x', y', z')$ should be

$$p' = pAB \tag{42}$$

After rotation, (37) becomes (43) shown at the top of the page.

As the cutting plane is just the *XY* plane ($z' = 0$) in Cartesian coordinates system and $\theta' = \frac{\pi}{2}$ in Spherical coordinate system

$$\begin{aligned} P_{\text{out}} &= \frac{\omega^2 I^2 (R_4 + R_{load})}{(R_4 + R_{load})^2 + X_4^2} \\ &\times \left( \left( \frac{acM_{14} - a^2 M_{34} + b\,(cM_{24} - bM_{34})}{\sqrt{a^2+b^2}\sqrt{a^2+b^2+c^2}} \right)^2 \right. \\ &\left. + \left( \frac{aM_{24} - bM_{14}}{\sqrt{a^2+b^2}} \right)^2 \right) \\ &\times \left( \sin \left( \arctan \left( \frac{acM_{14} - a^2 M_{34} + b\,(cM_{24} - bM_{34})}{\sqrt{a^2+b^2+c^2}(aM_{24} - bM_{14})} \right) + \varphi' \right) \right)^2 \\ &= K' \sin^2 (\gamma' + \varphi') \end{aligned} \tag{44}$$

where

$$\begin{aligned} K' = & \frac{\omega^2 I^2 (R_4 + R_{\text{load}})}{(R_4 + R_{\text{load}})^2 + X_4^2} \\ & \times \left( \left( \frac{acM_{14} - a^2 M_{34} + b\,(cM_{24} - bM_{34})}{\sqrt{a^2+b^2}\sqrt{a^2+b^2+c^2}} \right)^2 \right. \\ & \left. + \left( \frac{aM_{24} - bM_{14}}{\sqrt{a^2+b^2}} \right)^2 \right) \end{aligned} \tag{45}$$

$$\gamma' = \arctan \left( \frac{acM_{14} - a^2 M_{34} + b\,(cM_{24} - bM_{34})}{\sqrt{a^2+b^2+c^2}\,(aM_{24} - bM_{14})} \right) \tag{46}$$

Finally, after applying (27), the equation for $P_{\text{in}}$ in the rotated coordinates is

$$P_{\text{in}} = I^2 R + P_{\text{out}} \tag{47}$$

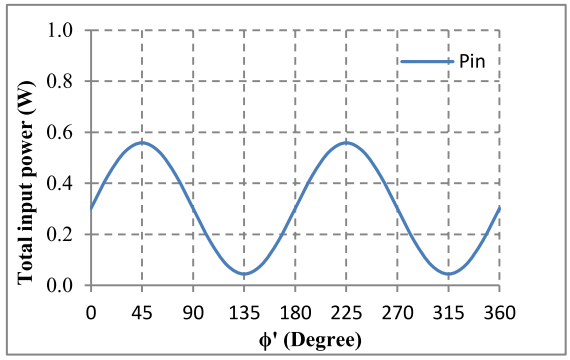


Fig. A1. Typical variation of the input power as a function of the angle of the magnetic vector $\varphi'$.

$$= I^2 R + K' * \sin^2 (\gamma' + \varphi')$$

where, $K'$ and $\gamma'$ are constants.

A typical input power curve $P_{\text{in}}$ as a function of $\varphi'$ is a sinusoidal waveform with a known offset $I^2 R$ as shown in Fig. A1. One can use only two measurements of total input power at different current vector angle $\varphi'_1, \varphi'_2$ to calculate $K'$ and $\gamma'$, and then predict the angle $\varphi'_m$ at which the maximum input power in the selected cutting plane occurs. From (11), (17), (27), and (30), the load power, output power (power picked up by the receiving coil), and the efficiency will reach their maximum point at the same angle $\varphi'_m$.

## REFERENCES

[1] J. S. Ho, S. Kim, and A. Poon, "Midfield wireless powering for implantable systems," *Proc. IEEE*, vol. 101, no. 6, pp. 1369–1378, Jun. 2013.
[2] S. Y. Hui, "Planar wireless charging technology for portable electronic products and Qi," *Proc. IEEE*, vol. 101, no. 6, pp. 1290–1301, Jun. 2013.
[3] G. A. Covic and J. T. Boys, "Inductive power transfer," *Proc. IEEE*, vol. 101, no. 6, pp. 1276–1289, Jun. 2013.
[4] W. Zhong, C. K. Lee, and S. Y. R. Hui, "General analysis on the use of Tesla's resonators in domino forms for wireless power transfer," *IEEE Trans. Ind. Electron.*, vol. 60, no. 1, pp. 261–270, Jan. 2013.
[5] S. Kung, B. Bae, J. J. Kim, S. Kim, D. H. Jung, and J. Kim, "Electromagnetic radiated emissions from a repeating-coil wireless power transfer system using a resonant magnetic field coupling," in *Proc. IEEE Wireless Power Transfer Conf.*, May 8–9 2014, pp. 138–141.
[6] K. O'Brien, "Inductively coupled radio frequency power transmission system for wireless systems and devices," Ph.D. dissertation, Technische Universitat Dresden, Dresden, Germany, 2006.
[7] O. Jonah, S. V. Georgakopoulos, and M. M. Tentzeris, "Orientation insensitive power transfer by magnetic resonance for mobile devices," in *Proc. IEEE Wireless Power Transfer*, Perugia, Italy, May 15–16, 2013, pp. 5–8.
[8] D. Wang, Y. Zhu, Z. Zhu, T. T. Mo, and Q. Huang, "Enabling multi-angle wireless power transmission via magnetic resonant coupling," in *Proc. 7th Int. Conf. Comput. Convergence Technol.*, Dec. 2012, pp. 1395–1400.

[9] M. J. Chabalko and A. P. Sample, "Three-dimensional charging via multimode resonant cavity enabled wireless power transfer," *IEEE Trans. Power Electron.*, vol. 30, no. 11, pp. 6163–6173, Nov. 2015.
[10] W. Ng, C. Zhang, D. Lin, and S. Y. R. Hui, "Two- and three-dimensional omni-directional wireless power transfer," *IEEE Trans. Power Electron.*, vol. 29, no. 9, pp. 4470–4474, Sep. 2014.
[11] C. Zhang, D. Lin, and S. Y. R. Hui, "Systems and methods for load position detection and power control of omni-directional wireless power transfer," PCT Patent Appl. PCT(CN2015(071 543, Jan. 26, 2015.
[12] C. Zhang, D. Lin, and S. Y. R. Hui, "Basic control principle of 3-dimensional omnidirectional wireless power transfer," *IEEE Trans. Power Electron.*, vol. 31, no. 7, pp. 5215–5227, Jul. 2016.
[13] Wikipedia, (2015, Aug.). [Online] Available: https://en.wikipedia.org/wiki/Spherical_coordinate_system] Spherical coordinate system
[14] S. Babic and C. Akyel, "Improvement in calculation of the self- and mutual inductance of thin-wall solenoids and disk coils," *IEEE Trans. Magn.*, vol. 36, no. 4, pp. 1970–1975, Jul. 2000.
[15] D. Lin, J. Yin, and S. Y. Hui, "Parameter identification of wireless power transfer systems using input voltage and current," in *Proc. IEEE Energy Convers. Congr. Expo.*, Sep. 2014, pp. 832–836.
[16] C. Zheng, D. Lin, and S. Y. R. Hui, "Omni-directional wireless power transfer systems using discrete magnetic field vector control," in *Proc. IEEE Energy Convers. Congr. Expo.*, Montreal, QC, USA, Sep. 2015, pp. 3203–3208.

**Deyan Lin** (M'09) was born in China, in 1972. He received the B.Sc. and M.A.Sc. degrees from the Huazhong University of Science and Technology, Wuhan, China, in 1995 and 2004, respectively, and the Ph.D. degree from the City University of Hong Kong, Kowloon Tong, Hong Kong, in 2012.

He is currently a Postdoctoral Fellow with the Department of Electrical and Electronic Engineering, The University of Hong Kong, Pokfulam, Hong Kong. From 1995 to 1999, he was a Teaching Assistant in the Department of Electrical Engineering, Jianghan University, Wuhan, where he became a Lecturer later. From 2008 to 2009, he was a Senior Research Assistant with the City University of Hong Kong. His current research interests include wireless power transfer, memristors and modeling, control, simulation of gas-discharge lamps.

**Cheng Zhang** (S'13) was born in China, in 1990. He received the B.Eng. (first class Hons.) degree in electronic and communication engineering from the City University of Hong Kong, Kowloon Tong, Hong Kong, in 2012, and is currently working toward the Ph.D. degree in the Department of Electrical and Electronic Engineering, The University of Hong Kong, Pokfulam, Hong Kong.

His current research interests include designs and optimizations for wireless power transfer applications.

**S. Y. Ron Hui** (M'87–SM'94–F'03) received the B.Sc.(Hons.) degree in engineering from the University of Birmingham, Birmingham, U.K., in 1984 and the D.I.C. and Ph.D. degrees from the Imperial College London, London, U.K., in 1987.

He is currently the Philip Wong Wilson Wong Chair Professor at the University of Hong Kong, Pok Fu Lam, Hong Kong, and a part-time Chair Professor at Imperial College London.

He has published more than 300 technical papers, including more than 200 refereed journal publications. More than 60 of his patents have been adopted by industry. His inventions on wireless charging platform technology underpin key dimensions of Qi, the world's first wireless power standard, with freedom of positioning and localized charging features for wireless charging of consumer electronics.

Dr. Hui is an Associate Editor of the IEEE TRANSACTIONS ON POWER ELECTRONICS and the IEEE TRANSACTIONS ON INDUSTRIAL ELECTRONICS, and an Editor of the IEEE JOURNAL OF EMERGING AND SELECTED TOPICS IN POWER ELECTRONICS. In November 2010, he received the IEEE Rudolf Chope R&D Award from the IEEE Industrial Electronics Society and the IET Achievement Medal (The Crompton Medal). He is a Fellow of the Australian Academy of Technology & Engineering and is the recipient of the 2015 IEEE William E. Newell Power Electronics Award.